Superhalogen Modulation: An Effective Approach for Minimizing Light-Induced Halide Segregation in $MAPb(I_{0.7}Br_{0.3})_3$

Pronoy Nandi,[1,3] Hyoungmin Park,[1,3] Sooeun Shin,[1,3] Anir S. Sharbirin,[1] Jeongyong Kim,[1] Seok Joon Kwon,[2,3] Nam-Gyu Park,[2,3] and Hyunjung Shin[1,3,*]

[1]Department of Energy Science, [2]School of Chemical Engineering, and [3]SKKU Institute of Energy Science and Technology (SIEST) Sungkyunkwan University, Suwon, Korea

Email: hshin@skku.edu

Experimental Details:

1) Materials:

All chemicals were used as received without further purification: methylammonium iodide (MAI, Greatcell Solar), lead iodide (PbI_2, 99.99%, Sigma-Aldrich), lead bromide ($PbBr_2$, 99.99%, sigma-Aldrich), Methylammonium tetrafluoroborate ($MABF_4$, 99.5%, Greatcell Solar), Formamidinium tetrafluoroborate ($FABF_4$, 99.5%, Greatcell Solar), Phenylammonium tetrafluoroborate ($PEABF_4$, 99.5%, Greatcell Solar), N,N-dimethylformamide (DMF, anhydrous 99.8%, sigma), dimethyl sulfoxide (DMSO, anhydrous 99.9%, sigma), Chlorobenzene (CB, anhydrous 99.8%, sigma) and fluorine-doped tin oxide conducting glass (FTO).

2) Perovskite Film Synthesis and Fabrication:

The $MAPbI_{2.1}Br_{0.9}$ perovskite films were prepared by dissolving the precursor salts in anhydrous N,N-dimethylformamide (DMF) and dimethyl sulfoxide (DMSO) mixture (8:1 volume ratio) to obtain a stoichiometric solution with the desired $MAPbI_{2.1}Br_{0.9}$ composition. 1.4 M precursor solution of Reference was prepared by dissolving 159 mg MAI, 165.2 mg $PbBr_2$ and 253.5 mg PbI_2 in DMF (634 µl) - DMSO (80 µl) mixture at room temperature under continuous stirring. Thereafter, $MAPbI_{2.1}Br_{0.9}$+x $MABF_4$, $MAPbI_{2.1}Br_{0.9}$+x $FABF_4$, and $MAPbI_{2.1}Br_{0.9}$+x $PEABF_4$ (x= 0.1%, 0.3%, 0.5%, 0.8%, 1%, 2%) samples were prepared by adding stoichiometric amount of $MABF_4$, $FABF_4$ and $PEABF_4$ with the Reference solution and termed them as Target0, Target1 and Target2,

respectively. In order to grow thin films, FTO substrates of dimension 2 cm × 2 cm were cleaned by sequential sonication in soap solution, millipore water, ethanol, followed by drying in Ar flow and finally UV-Ozone treatment (Ossila, UK) for 10 minutes. Then the perovskite precursor solutions were spincoated at 5000 rpm 40 seconds. An antisolvent (300 µl chlorobenzene) was dispensed on perovskite film 15 seconds before the end of spinning program to obtain an adduct film. The adduct films were then annealed at 100 °C on a hotplate for 20 min. The spin-coating and annealing processes were conducted in an argon-filled dry box (H_2O and O_2 concentrations < 1 ppm). Spin-coating and annealing process is also same for $MABF_4$, $FABF_4$, and $PEABF_4$ incorporated films.

3) <u>Characterization:</u>

(i) <u>X-ray diffraction and field emission scanning electron microscopy</u>: Powder X-ray diffraction of bulk and thin film samples were performed in Bruker D8 Advance X-ray diffractometer using Cu K_α radiation (λ = 1.5406 Å). Film morphology, grain size of Reference, Target1 and Target2 samples were characterized using field emission scanning electron microscope (FESEM; Neon 40 cross-beam system, MS Carl Zeiss GmbH); whereas the halide composition of the above films were extracted from Energy disperse x-ray spectroscopy (EDS) measurement equipped with FESEM.

(ii) <u>X-ray Photoelectron Spectroscopy (XPS)</u>: X-ray Photoelectron Spectroscopy (XPS) measurements were performed on AXIS SUPRA (Kratos, U.K) XPS Microprobe using monochromatic Al K_α radiation (1.487 keV) at room temperature. The base pressure during spectra acquisition was better than $5x10^{-10}$ torr. The excitation source was Al K (1.487 keV) operated at 300 Watt. The spectra were acquired sequentially and charge extractor was used to minimize the chemical shift. Also the spectrum were calibrated with reference to the adventitious C 1*s* peak at 284.8 eV.

(iii) <u>Steady-state absorption measurements and Rate constant calculation:</u> Steady-state absorption measurements of all the samples were carried out using a Varian Cary 50 bio spectrophotometer in the wavelength region of 500–850 nm at ambient condition. A continuous wave (CW) LED lamp with an excitation intensity of 150 mW/cm^2 (Figure S3) was used to shine light on all the perovskite films to identify Photoinduced phase segregation. The difference absorption (ΔA) spectra were obtained by subtracting the spectrum at 0 s as a reference from the spectra acquired at a later time. The halide segregation kinetics was probed using absorption changes at the mixed halide, I-rich and

Br-rich regions as we continued to photo-irradiate all the samples. These traces were then fitted using the first order kinetics (mono exponential fit).[1] Here we fitted the data using the relation: $[\Delta A] = [\Delta A]_0 \exp(-kt)$, where $[\Delta A]$ is the change in absorption at time t and $[\Delta A]_0$ is the change in absorption at time t = 0, and k is the first-order rate constant. Here we have fixed $[\Delta A]_0 = 0.001$ and fitted all the data using above equation. All the mono exponential decay or growth fits well with reduced R^2 in the range between 0.988 and 0.995.

(iv) Photoluminescence (PL) Measurement: The confocal PL was measured using a lab made laser confocal microscope combined with a spectrometer. An argon laser with an excitation wavelength of 514 nm was employed for confocal PL measurements. The laser light was focused using an objective lens (100x, 0.95 NA), and the scattered light was collected using the same objective lens and then guided to a 50 cm long monochromator equipped with a cooled charge-coupled device (CCD) (PIXIS 400, Princeton Instruments). The piezo stages are moved in x and y direction for a confocal PL mapping measurement. The image size was 20x20 μm with 64x64 pixel. The PL spectrum at each pixel was taken with an exposure time of 0.05s.

(v) Thermal admittance spectroscopy (TAS): The TAS measurements were performed by using a HewLett Packard 4284A Precision LCR Meter. For the TAS measurement, the direct current bias (V) was fixed at 0 V and the amplitude of the alternating current bias (δV) was 50 mV. The scanning range of the alternating current frequency (f) was 20 Hz to 1 MHz. Capacitance (*C) vs* Frequency (*F)* and Capacitance *(C) vs* Voltage (*V)* responses of the device are measured in dark to calculate the defect DOS (as given in figures 5). Decrease in the effective C with increasing V (Figure S10 (a)) attributes to the decreased barrier potential as a consequence of increased V_{bi} value. Also, applied voltage would be in the opposite direction to the field of V_{bi}. Figure S10(b) shows the Mott-Schottky analysis for the studied Reference, Target1 and Target2 samples from which V_{bi} has been extracted.[2]

Trap density of states (tDOS) variation is calculated by performing the *C–F* measurement in the dark, which has contribution only from the defects. As shown in Figure S11, reduction in the low frequency capacitance suggests a decrement in the defects states. Trap states located in the mid gap used to respond to capacitance depending upon their energy and space position. Now if we consider a defect level which coincides

with the Fermi energy within the band gap because of the band bending, then the states at this certain position in the band gap will respond for the energy which is having higher value than them. This energy is generated from a small ac signal with the frequency ω and this energy is termed as demarcation energy and is given by[2,3]:

$$E_\omega = K_B T \ln\left(\frac{\omega_0}{\omega}\right)$$

Here ω_0 is the attempt to escape angular frequency, ω is the angular frequency of ac modulation, T is the temperature, and $K_B$is the Boltzmann constant. The capacitance response will only be observed for the trap states which are lying below a certain demarcation energy. This generates the spectrum for the trap energies lying in the band gap. The energy distribution and tDOS ($N_T(E_\omega)$) are deduced from capacitance measurements using the derivative of capacitance with respect to angular frequency of the applied ac signal which is expressed as

$$N_T(E_\omega) = -\frac{1}{qK_BT}\,\frac{\omega dC}{d\omega}\,\frac{V_{bi}}{W}$$

Here q, K_B, T, ω and C are elementary charge, Boltzmann's constant, temperature, angular frequency and specific capacitance, respectively; W and V_{bi} are the depletion width (taken as 1000 μm) and build-in potential (calculated from Mott-Schottky analysis), respectively. Temperature-dependent capacitance measurements were performed in a MS TECH probe station with a hot chuck Controller (MST-1000B).

(vi) Crystalline growth mechanism study: Nucleation and growth rates of Reference, Target 0, Target1 and Target2 were studied using optical microscope (Olympus; BH2-UMA).

4) Perovskite Solar Cell (PSC) device fabrication and characterization:

Patterned Fluorine-doped tin oxide (FTO) glass substrates were rinsed by sonication in detergent (5 wt% Hellmanex III in ultra-pure water) and then cleaned with ultra-pure water, acetone and ethanol for 20 min each, respectively. Thereafter FTO substrates were treated in a UV-Ozone cleaner (Ossila, UK) for 15 min and transferred to the Atomic Layer Deposition (ALD) chamber to prepare ultrathin NiO film. The preparation of NiO by ALD was described in detailed in our previous work.[4–6] In short, the ALD-NiO deposition process was conducted with flow-type ALD equipment

(LUCIDA-D100, NCD, Republic of Korea). For ALD precursor, namely, MABON ((1-dimethylamino-2-methyl-2-butoxide)Nickel(II), DNF, Republic of Korea) and Ozone generated by ozone generator (LAB-II, Ozonetech, Republic of Korea) used as a metal and oxygen precursor each respectively. The reaction chamber was kept at 200℃ and MABON was evaporated at 65℃. Thereafter, the NiO deposited films were annealed in box furnace at the ambient air (at 300℃ for 1 hour). Annealed NiO-deposited FTO substrates were immediately transferred into an argon-filled glove box for deposition of the self-assembled monolayers (SAMs) which form layers by the self-assembly of surfactant molecules at surfaces as discussed in the literature.

In our case, SAM preparation utilized (2-(9H-carbazol-9-yl)ethyl)phosphonic acid [2PACz] (TCI, >98.0%) (6 mg) dissolved in 18 mL of ethanol as discussed in the literature.[7] Extra care was taken to prevent particle formation, whereby all solutions were prepared inside a glovebox and filtration was carried out using 0.2 μm syringe filters. Next, 2PACz was spin coated over NiO HTL at 4000 rpm for approximately 60 second followed by annealing at 100 °C for 10 min. Then the SAM deposited NiO films were washed using ethanol two times and annealed at 100 °C for 10 min.

The perovskite film deposition entailed two steps, starting with precursor solution preparation, followed by spinning. Details of precursor solution preparation is discussed in Perovskite film synthesis section. As prepared perovskite precursor solutions were then spin coated onto 2PACz/NiO/FTO substrates at 5000 rpm 40 seconds. An antisolvent (300 μl chlorobenzene) was dispensed on perovskite film 15 seconds before the end of spinning program to obtain an adduct film. The adduct films were then annealed at 100 °C on a hotplate for 20 min. The spin-coating and annealing processes were conducted in an argon-filled dry box (H_2O and O_2 concentrations < 1 ppm). Then Perovskite/2PACz/NiO/FTO are transferred to C60-BCP deposition chamber (Daedong High Technologies, Rep. of Korea) for electron transport layer deposition. Finally, C60 (25nm) and Bathocuproine (BCP, 6nm) was deposited under high vacuum ($<3.0 \times 10^{-6}$ torr) with 0.2Å/sec deposition rate. After deposition of C60/BCP layer, a 100 nm thick Ag was thermally evaporated under high vacuum ($<3.0 \times 10^{-6}$ Torr).

Current density (J) *vs.* Voltage (V) measurements of solar cell devices were performed using a Keithley 2400 source meter under the simulated AM 1.5G one sun illumination (100 mW cm^{-2}) using a solar simulator (Oriel Sol 3A class AAA) equipped with 1600 W Xenon lamp (Newport 94083A) and calibrated using NREL-calibrated Si reference cell with KG-5 filter (PV measurements). The illuminated area of the device was fixed at 0.06 cm^2 with a metal shadow mask during the

measurement. All PV cells were measured in ambient without any encapsulation at a scan rate of 50 mV/s from -0.2V to +1.25V. Light-illumination aging was performed under continuous 1 sun-equivalent illumination (100 mW cm^{-2}) without UV filter at room temperature in ambient air (the relative humidity was between 50% to 70%), and their performances were evaluated by the corresponding J–V scanning curves.

5) Computational Details:

To investigate the light-switching-derived segregation of the halide ions, we studied the phase separation dynamics in the lead halide perovskite film incorporated with the transport of polaron. For the simulation model, we employed a 2D stochastic simulation based on kinetic Monte Carlo (KMC) method on the 2D discrete square lattice. For the discrete model, we employed 120-by-120 2D square lattice cells, in which initial fraction of I and Br ions are given with Gaussian errors. On the lattice, we only considered short-range interaction potential between halide ions and charge carriers in the nearest neighboring cells. For polaron, we assumed that quadratic and symmetric strain profile ranging over 9 lattice cells. For the potential profile, we considered halide ion-polaron interaction driven by spatial gradient of the chemical potential (concentration-dependent diffusion), carriers-halide ion interaction driven by bandgap funnel (spatial gradient of valence bands edge), and carriers-polaron interaction driven by strain energy gradient (lattice cell perturbation by the polaron). For the last driving force, we considered local deformation of unit lattice-derived unbalanced distribution of carriers. The overall density of carriers in the film is controlled by the photo-excitation. The polaron, which is expected to form via local electrostatic interaction between charge carrier and halide ions in the unit cell, plays critical role when phonon vibration energy is comparable to the kinetic energy of the charge carriers. To simplify the 2D discrete model, we assumed that the cut off range (i.e., effective radius) of the polaron which can perturb the distribution of the ions and charge carriers is 2.5-times lattice constant. For the calculation of exchange of halide ions between the neighboring lattice cells, we calculated the stochastic waiting time for each jumping according to the free energy-dependent thermodynamic probability per Gillespie algorithm.[8] The waiting times of each of the cells are updated and heap sorted to track the dynamics of the halide ion segregation as well as track the overall free energy change over the system. The KMC with free-energy dependent probability was implement with Gibson-Bruck algorithm in conjunction with next-reaction algorithm for faster calculations.[9]

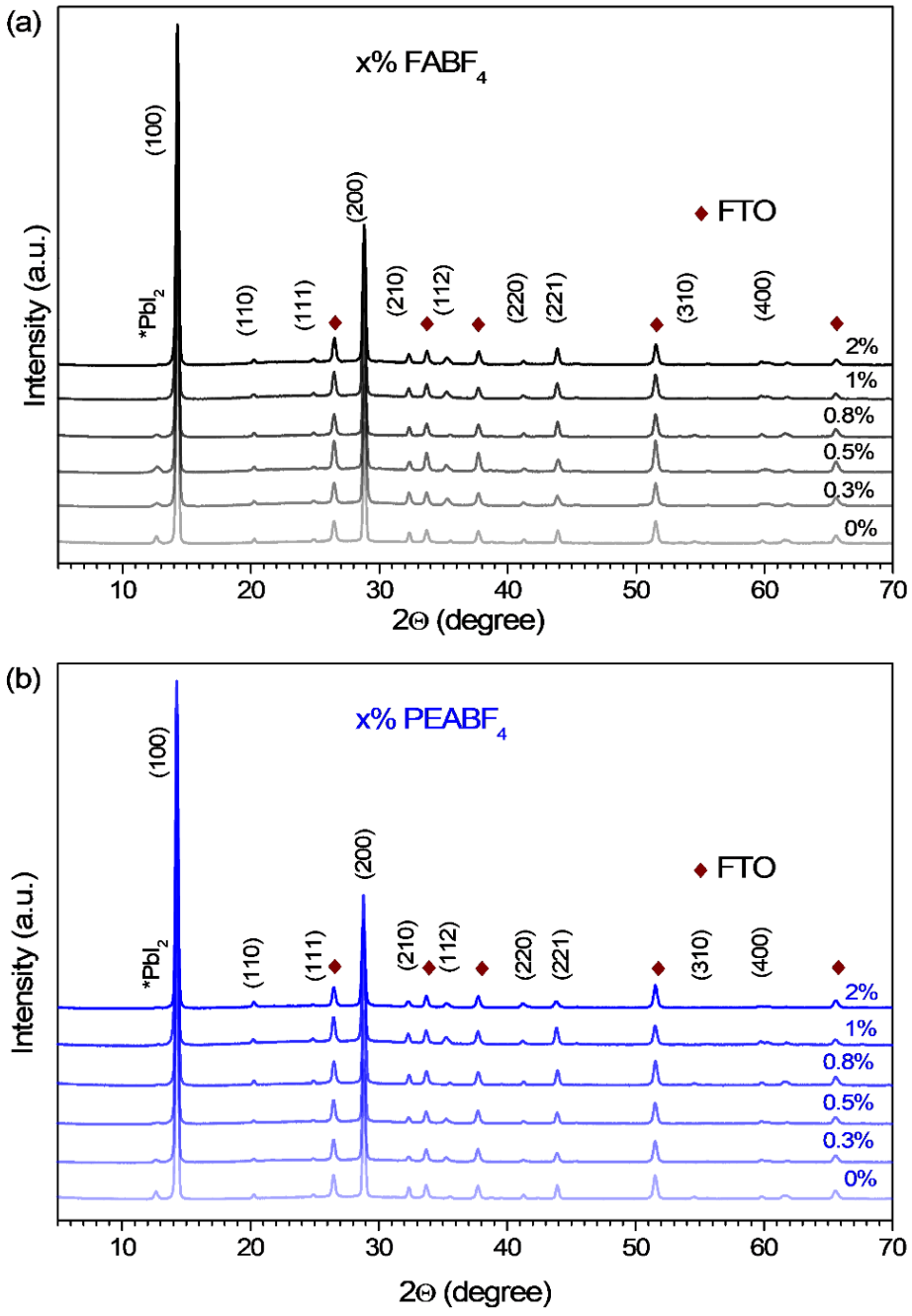

Figure S1: X-ray diffraction (XRD) patterns of (a) $MAPbI_{2.1}Br_{0.9}$ + x% $FABF_4$ (x= 0, 0.3, 0.5, 0.8, 1, 2) and (b) $MAPbI_{2.1}Br_{0.9}$ + x% $PEABF_4$ (x= 0, 0.3, 0.5, 0.8, 1, 2) films on FTO substrates.

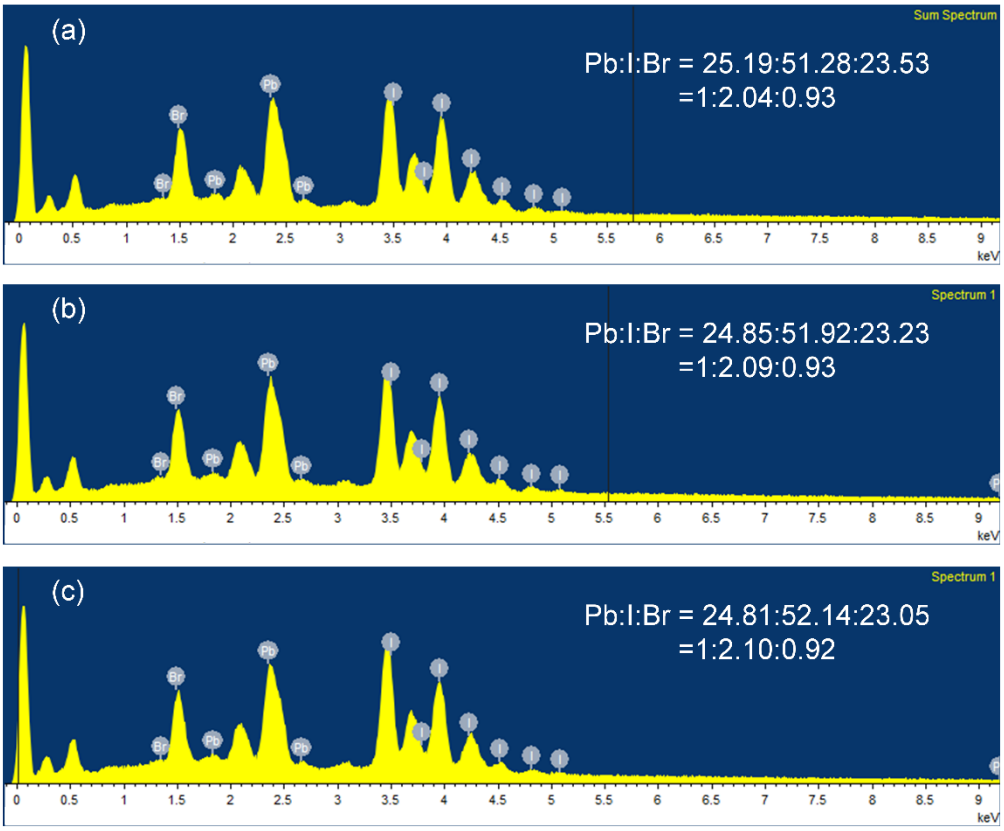

Figure S2: EDS spectra of (a) $MAPbI_{2.1}Br_{0.9}$ (Reference), (b) $MAPbI_{2.1}Br_{0.9}$ + 0.8% $FABF_4$ (Target 1) and (c) $MAPbI_{2.1}Br_{0.9}$ + 0.8% $PEABF_4$ (Target 2) films on FTO substrates

(a) $MAPbI_{2.1}Br_{0.9}$ (Reference)

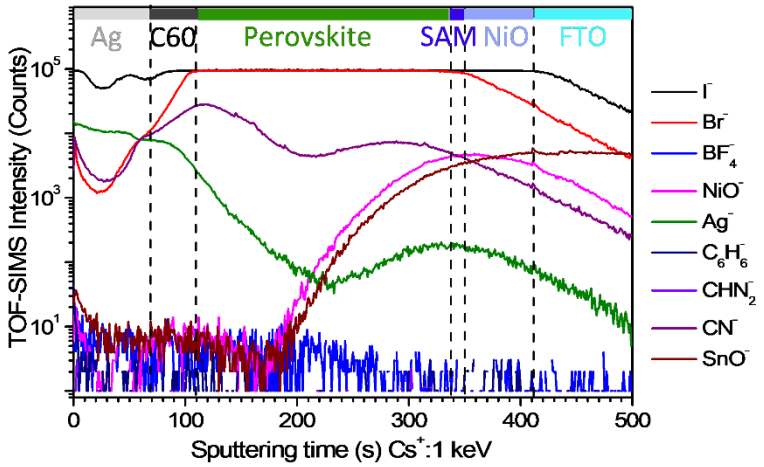

(b) $MAPbI_{2.1}Br_{0.9}$ +0.8%$FABF_4$ (Target1)

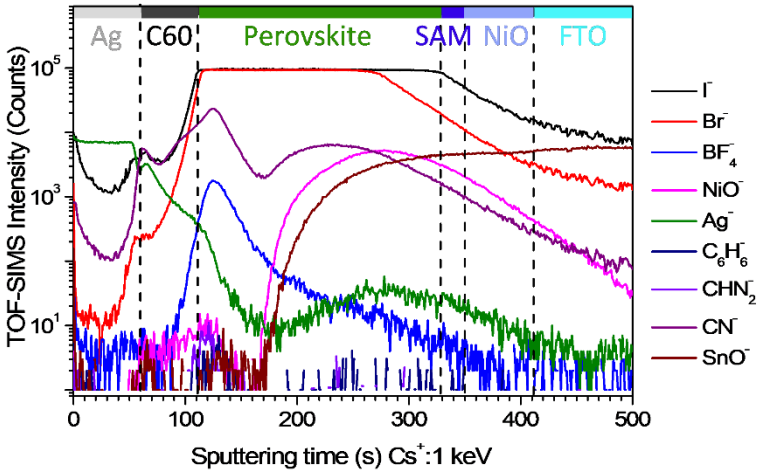

(c) $MAPbI_{2.1}Br_{0.9}$ +0.8%$PEABF_4$ (Target2)

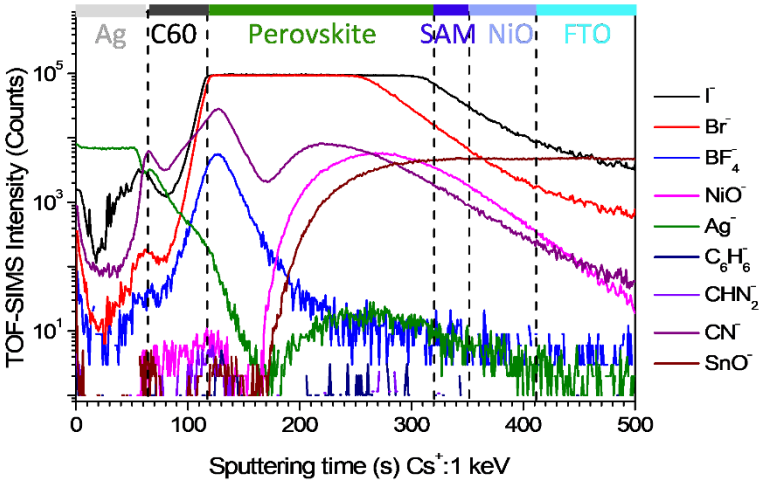

Figure S3: Time-of-flight secondary ion mass spectrometry (TOF-SIMS) depth profiles acquired on Ag/C60/Perovskite/SAM/ALD-NiO/FTO devices. (a) $MAPbI_{2.1}Br_{0.9}$ (Reference), (b) $MAPbI_{2.1}Br_{0.9}$ + 0.8% $FABF_4$ (Target 1) and (c) $MAPbI_{2.1}Br_{0.9}$ + 0.8% $PEABF_4$ (Target 2) films on FTO substrates.

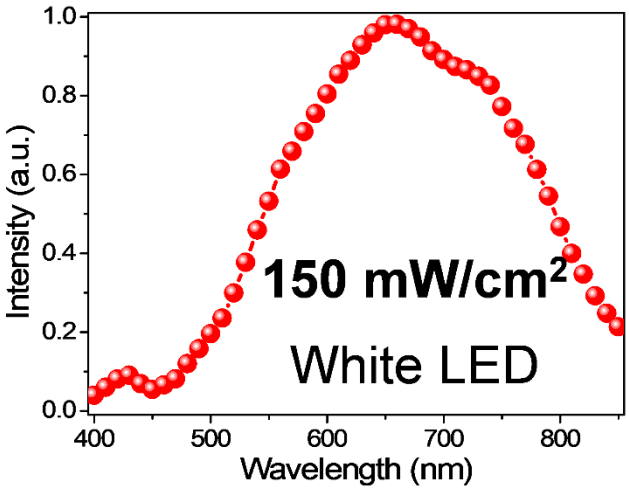

Figure S4: Normalized illumination spectrum of the XD 300, 250 Watt white LED excitation at 150 $mWcm^{-2}$ used to illuminate films.

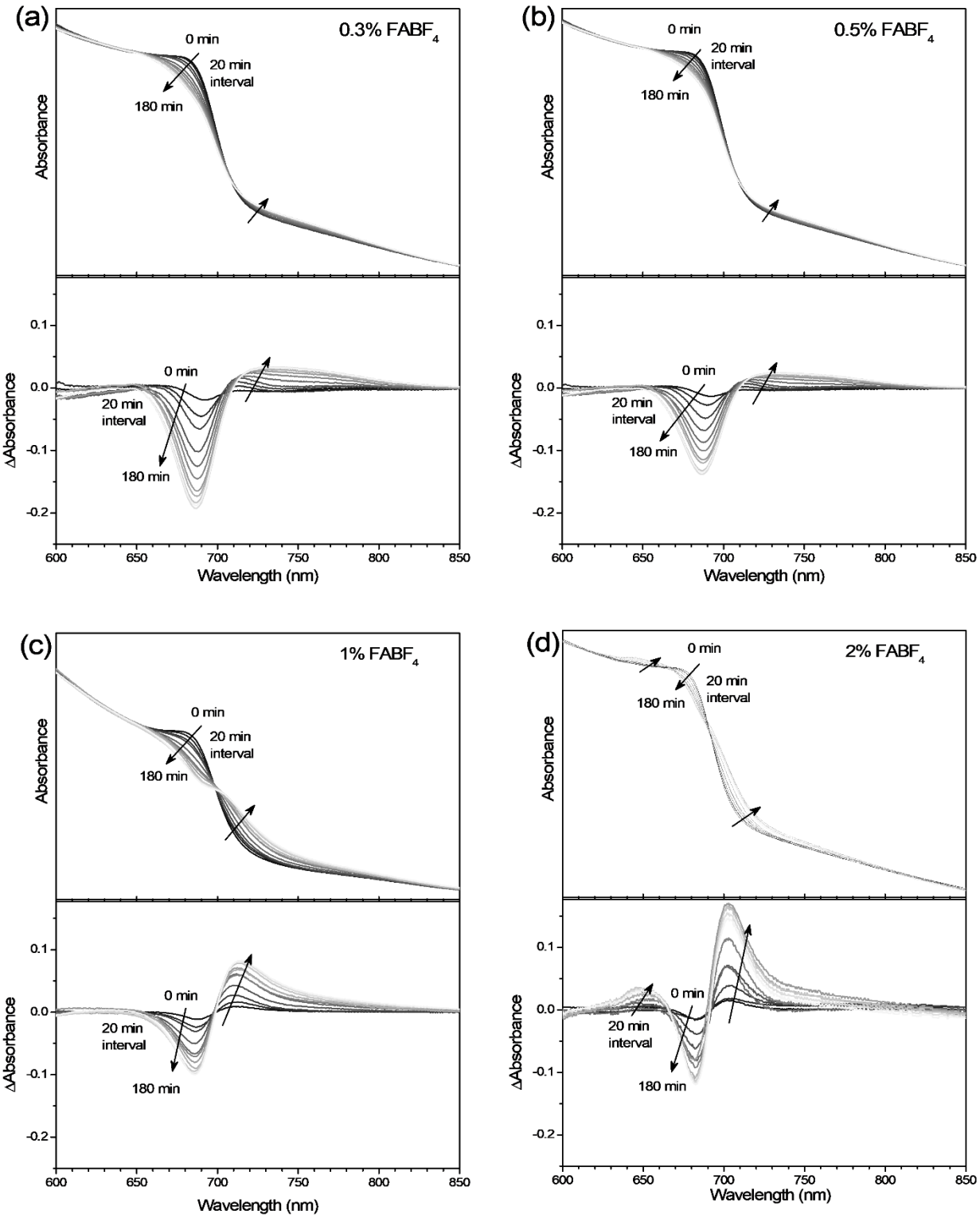

Figure S5: Absorption spectra (upper panel) and difference absorption spectra (lower panel) of (a) $MAPbI_{2.1}Br_{0.9}$ + 0.3% $FABF_4$, (b) $MAPbI_{2.1}Br_{0.9}$ + 0.5% $FABF_4$, (c) $MAPbI_{2.1}Br_{0.9}$ + 1% $FABF_4$, (d) $MAPbI_{2.1}Br_{0.9}$ + 2% $FABF_4$ films on FTO substrates. Here difference absorption spectra was obtained by subtracting the spectrum with no light spectrum.

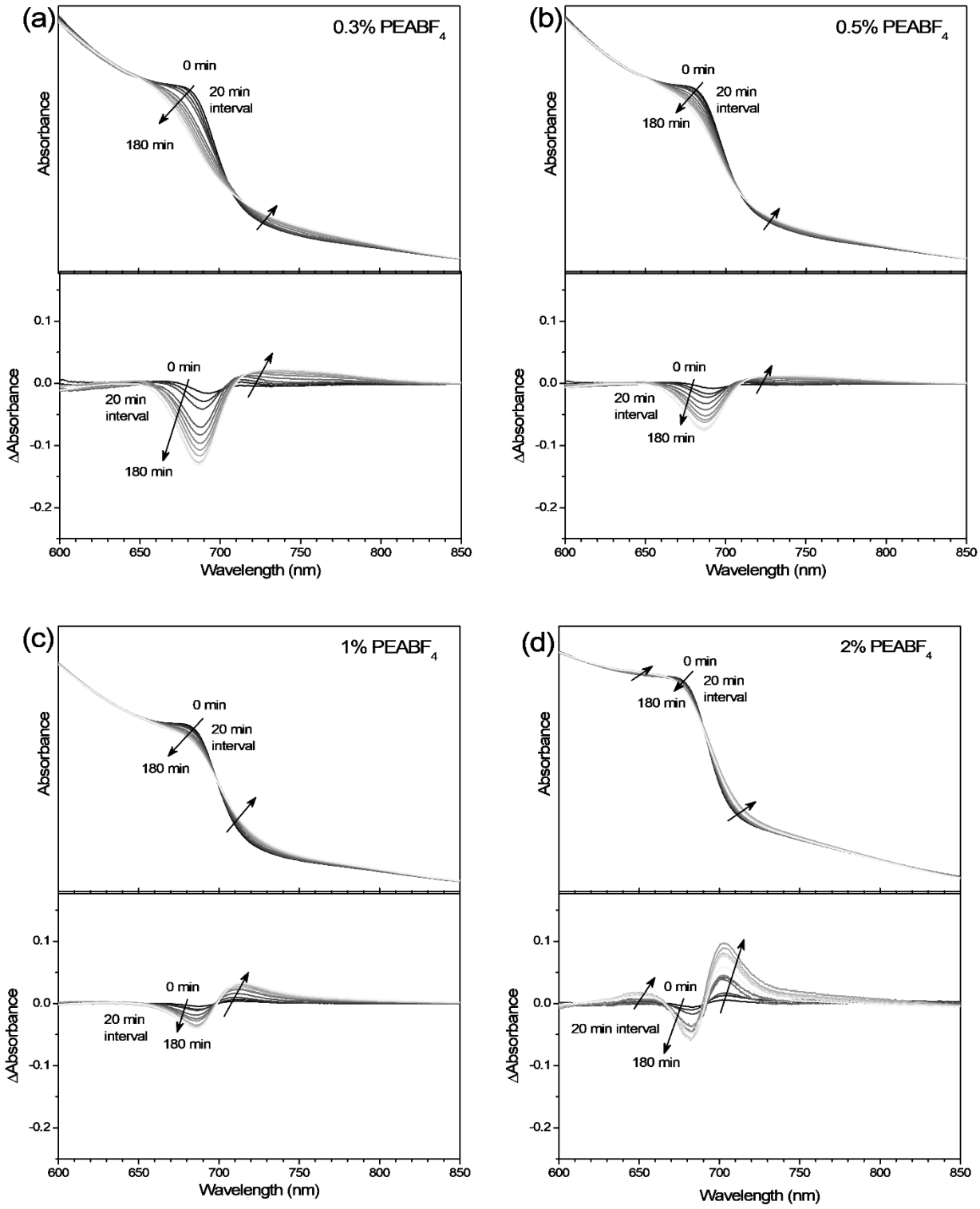

Figure S6: Absorption spectra (upper panel) and difference absorption spectra (lower panel) of (a) $MAPbI_{2.1}Br_{0.9}$ + 0.3% $PEABF_4$, (b) $MAPbI_{2.1}Br_{0.9}$ + 0.5% $PEABF_4$, (c) $MAPbI_{2.1}Br_{0.9}$ + 1% $PEABF_4$, (d) $MAPbI_{2.1}Br_{0.9}$ + 2% $PEABF_4$ films on FTO substrates. Here difference absorption spectra was obtained by subtracting the spectrum with no light spectrum.

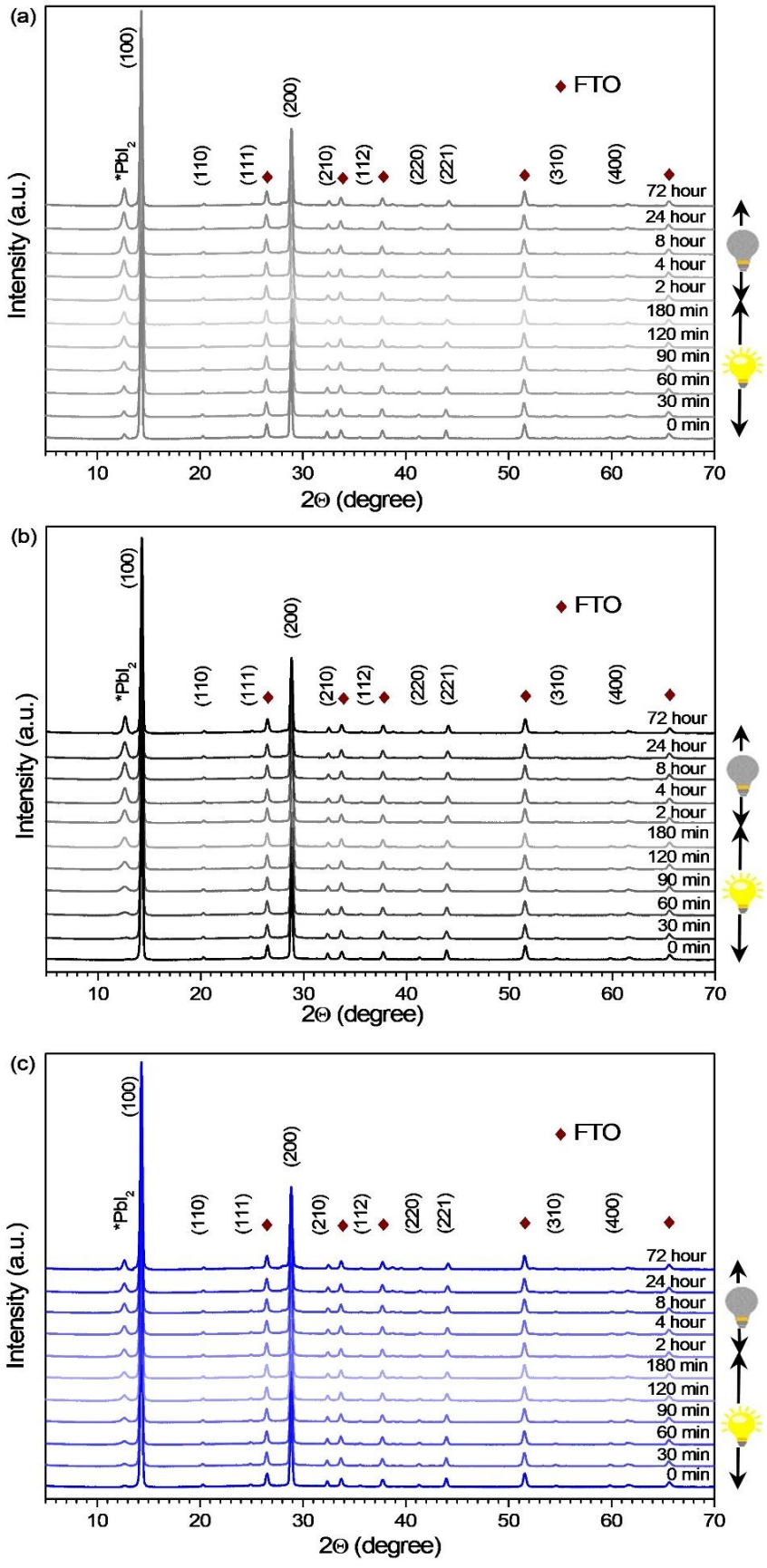
(a)
(b)
(c)
Intensity (a.u.)
2Θ (degree)
*PbI2
(100)
(110)
(111)
(200)
(210)
(112)
(220)
(221)
(310)
(400)
FTO
72 hour
24 hour
8 hour
4 hour
2 hour
180 min
120 min
90 min
60 min
30 min
0 min
10
20
30
40
50
60
70

Figure S7: XRD patterns of (a) $MAPbI_{2.1}Br_{0.9}$ (Reference; gray), (b) $MAPbI_{2.1}Br_{0.9}$ + 0.8% $FABF_4$ (Target 1; black) and (c) $MAPbI_{2.1}Br_{0.9}$ + 0.8% $PEABF_4$ (Target 2; blue) films on FTO substrates under continuous illumination till 3 hours and then aging in dark upto 72 hours.

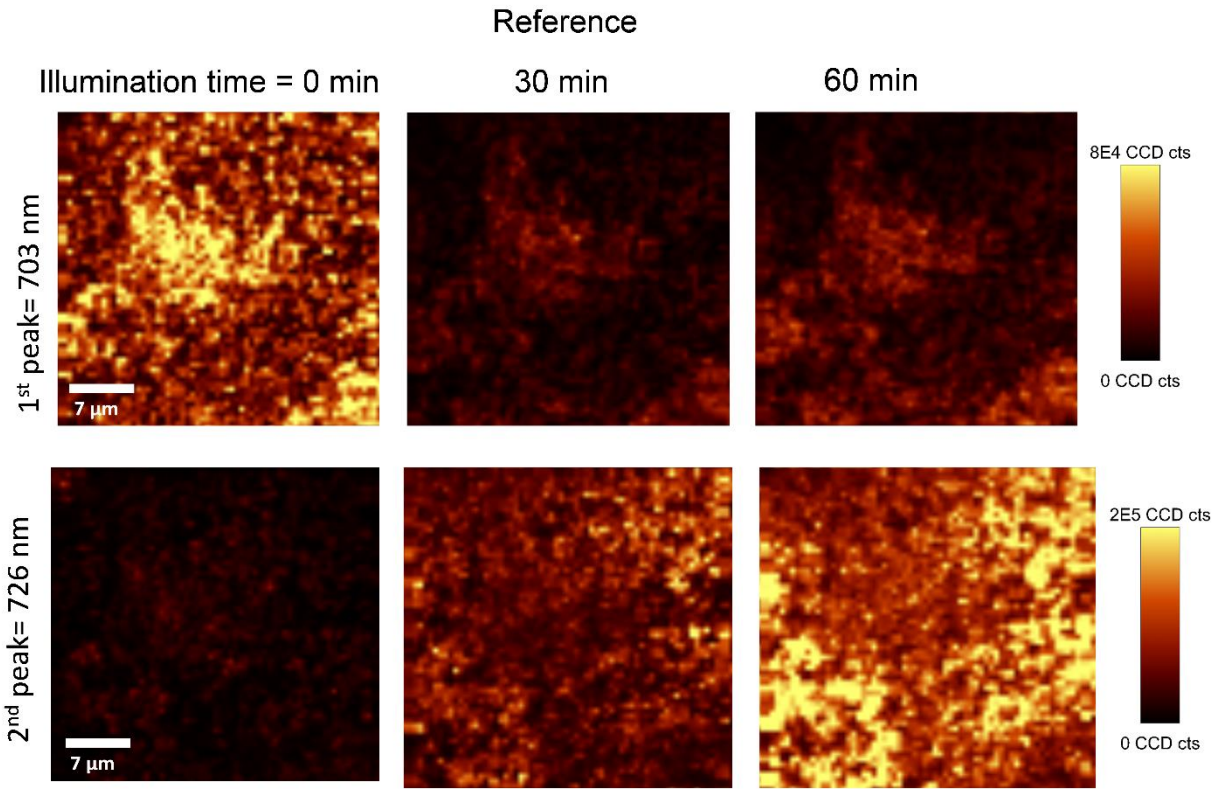

Figure S8: Confocal PL maps of $MAPbI_{2.1}Br_{0.9}$ (Reference) thin film on FTO substrate for different illumination time (0 min to 60 minute). Upper panel shows the evolution of peak 1 wavelength region (original mixed phase; 703 nm), whereas lower panel depict peak 2 wavelength region (segregated I-rich domains; 726 nm).

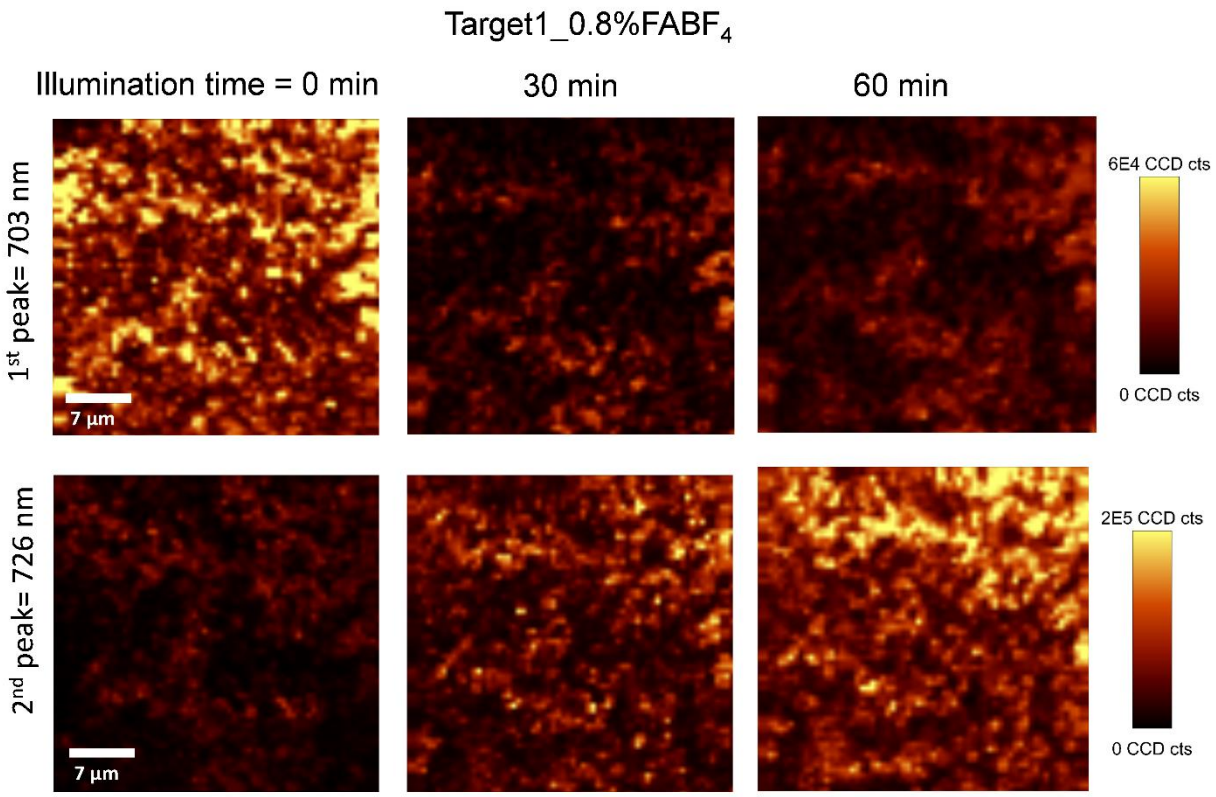

Figure S9: Confocal PL maps of $MAPbI_{2.1}Br_{0.9}$ + 0.8% $FABF_4$ (Target 1) thin film on FTO substrate for different illumination time (0 min to 60 minute). Upper panel shows the evolution of peak 1 wavelength region (original mixed phase; 703 nm), whereas lower panel depict peak 2 wavelength region (segregated I-rich domains; 726 nm).

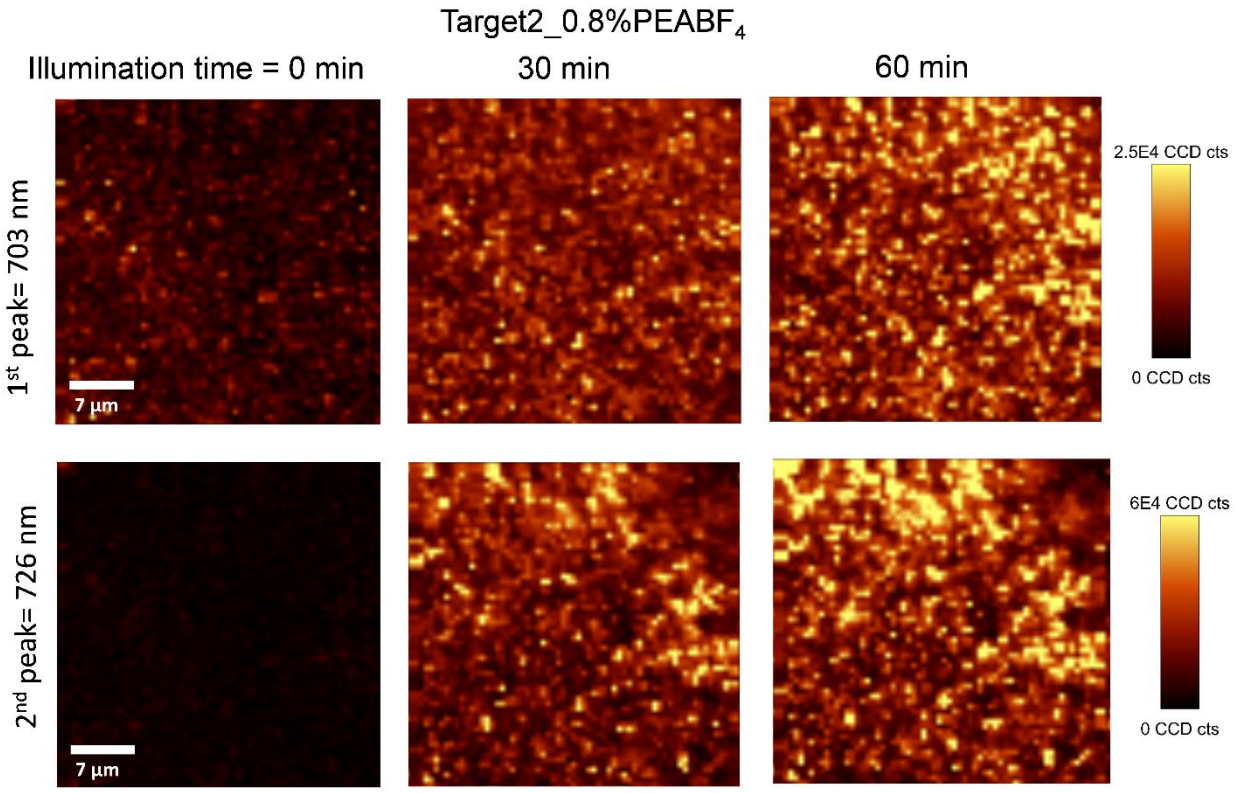

Figure S10: Confocal PL maps of $MAPbI_{2.1}Br_{0.9}$ + 0.8% $PEABF_4$ (Target 2) thin film on FTO substrate for different illumination time (0 min to 60 minute). Upper panel shows the evolution of peak 1 wavelength region (original mixed phase; 703 nm), whereas lower panel depict peak 2 wavelength region (segregated I-rich domains; 726 nm).

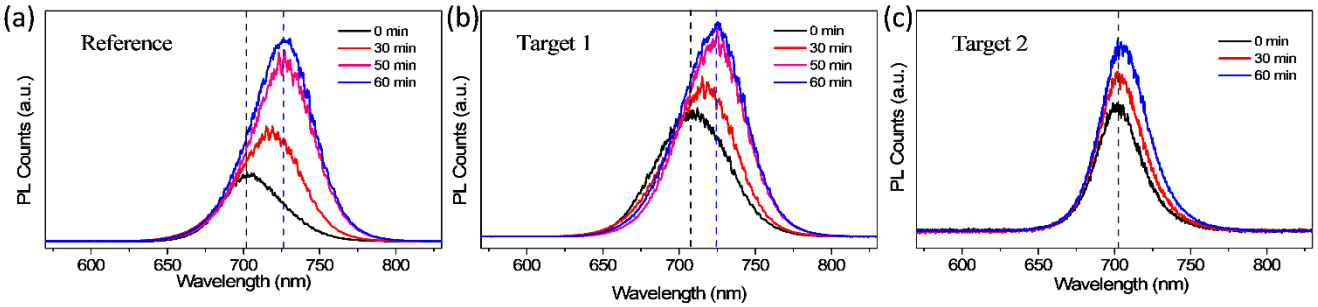

Figure S11: PL spectra of (a) $MAPbI_{2.1}Br_{0.9}$ (Reference); (b) $MAPbI_{2.1}Br_{0.9}$ + 0.8% $FABF_4$ (Target 1); (c) $MAPbI_{2.1}Br_{0.9}$ + 0.8% $PEABF_4$ (Target 2) thin film on FTO substrate for different illumination time (0 min to 60 minute). PL peak position before illumination and after 60 min continuous illumination are shown using black and blue dotted lines.

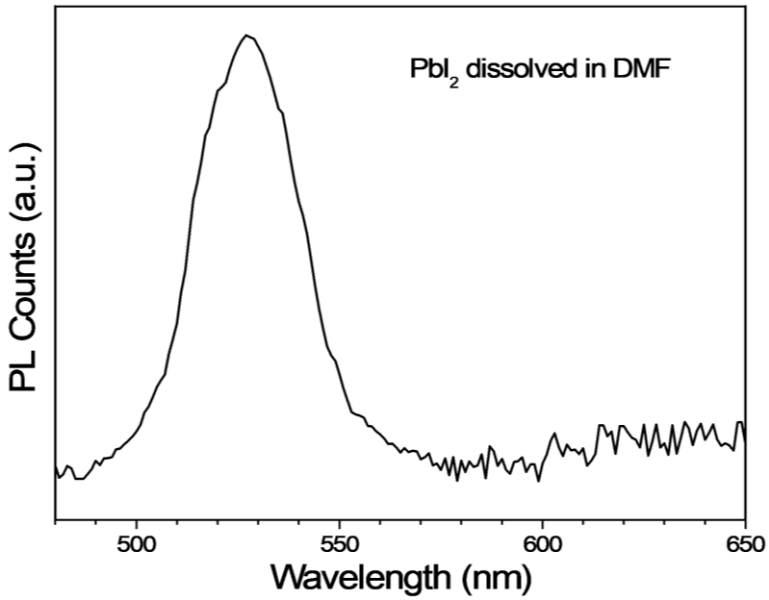

Figure S12: PL spectra of PbI_2 thin film on FTO substrate.

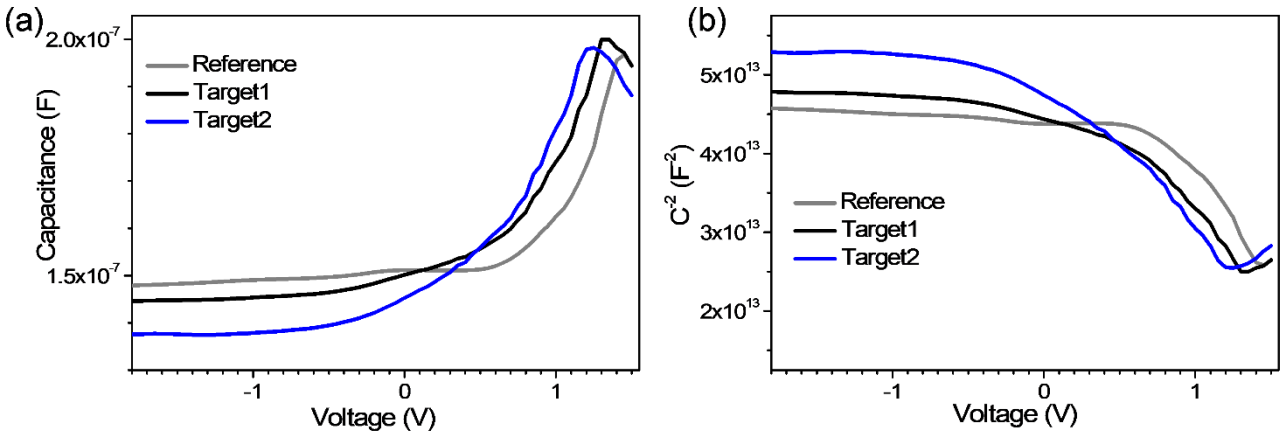

Figure S13: (a) Capacitance (C) *vs.* Voltage (V) characteristics and (b) Mott-Schottky plots (C^{-2} vs V) of $MAPbI_{2.1}Br_{0.9}$ (Reference; gray), $MAPbI_{2.1}Br_{0.9}$ + 0.8% $FABF_4$ (Target 1; black) and $MAPbI_{2.1}Br_{0.9}$ + 0.8% $PEABF_4$ (Target 2; blue) films on FTO substrates.

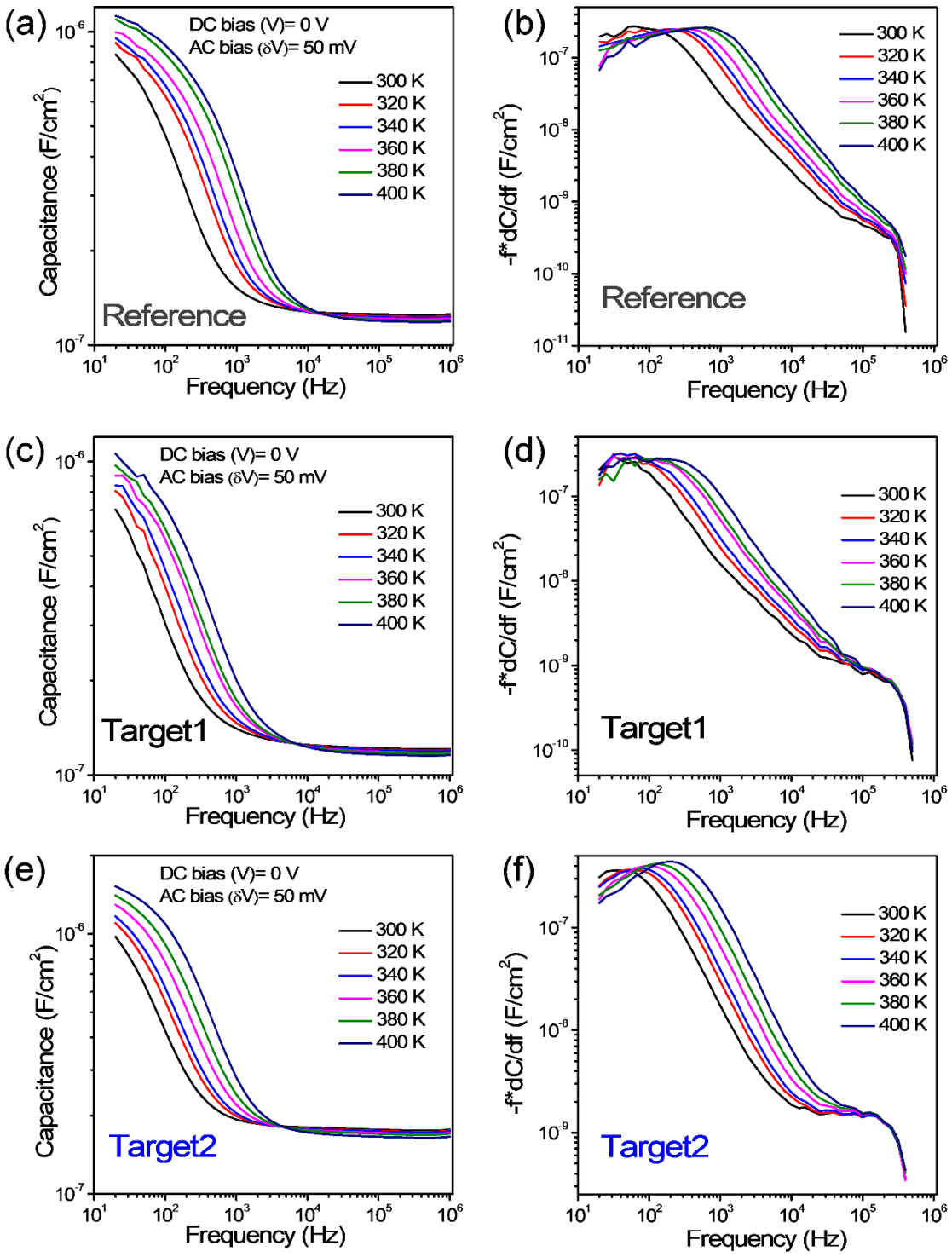

Figure S14: Thermal Admittance Spectroscopy Results of (a, b) $MAPbI_{2.1}Br_{0.9}$ (Reference; gray), (c, d) $MAPbI_{2.1}Br_{0.9}$ + 0.8% $FABF_4$ (Target 1; black) and (e, f) $MAPbI_{2.1}Br_{0.9}$ + 0.8% $PEABF_4$ (Target 2; blue) films on FTO substrates. (a, c, e) Capacitance (C) *vs.* Frequency (f) characteristics and (b, d, f) -f·dC/df *vs.* f curves.

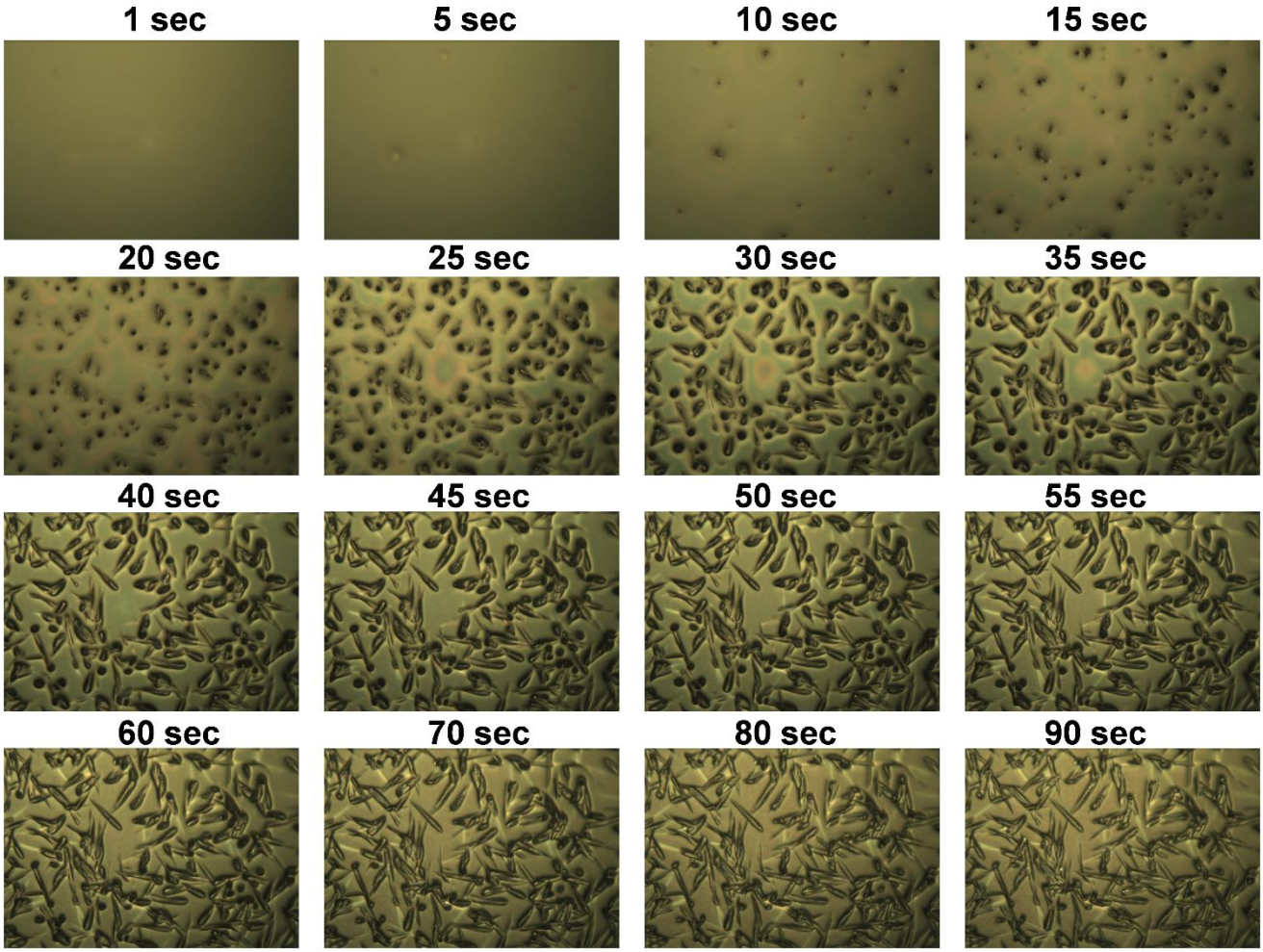

Figure S15: In-situ optical microscopy. Top-view optical microscope images of $MAPbI_{2.1}Br_{0.9}$ (Reference) film at various stages of isothermal crystallization.

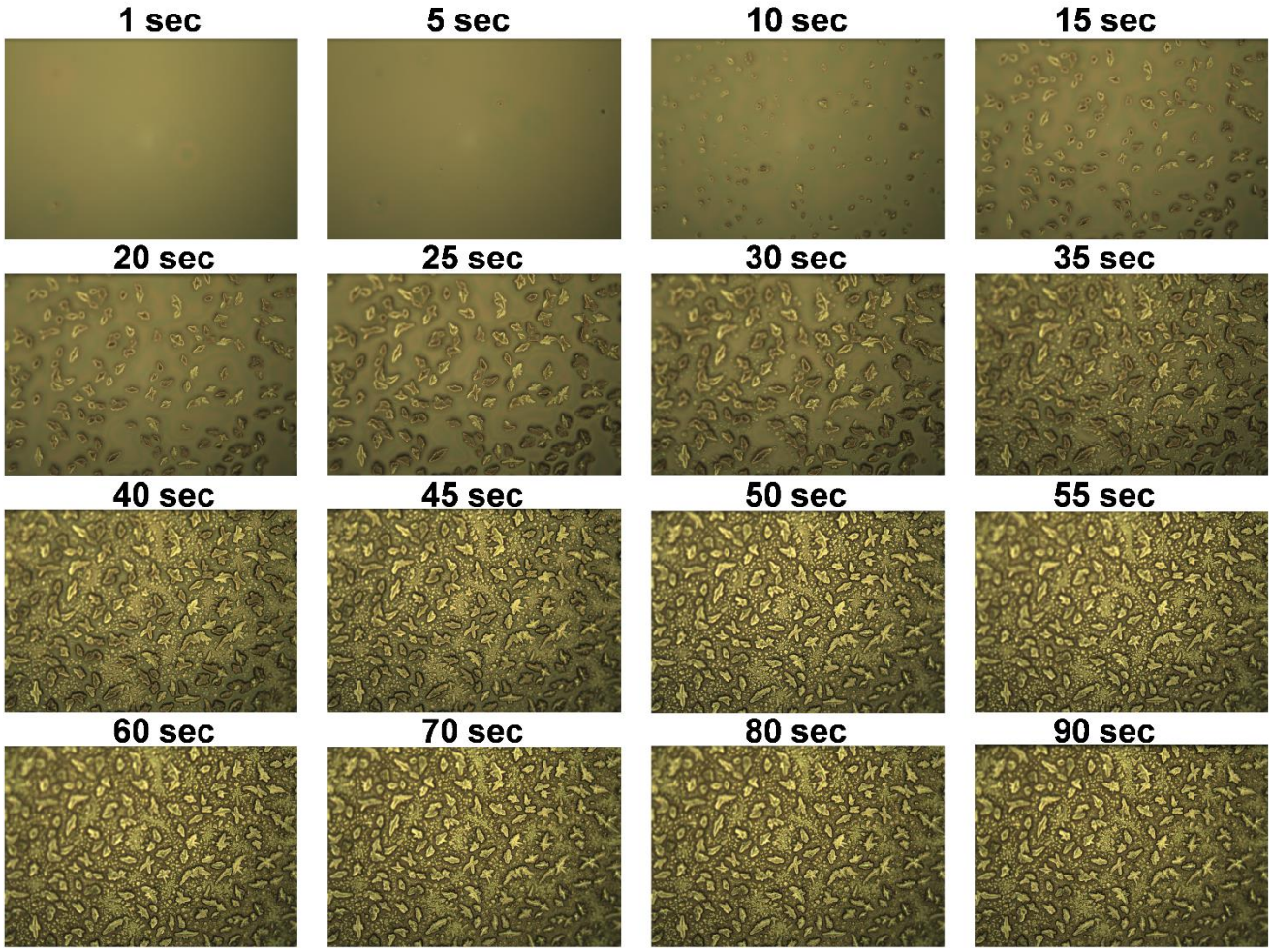

Figure S16: In-situ optical microscopy. Top-view optical microscope images of $MAPbI_{2.1}Br_{0.9}$ + 0.8% $MABF_4$ (Target 0) film at various stages of isothermal crystallization.

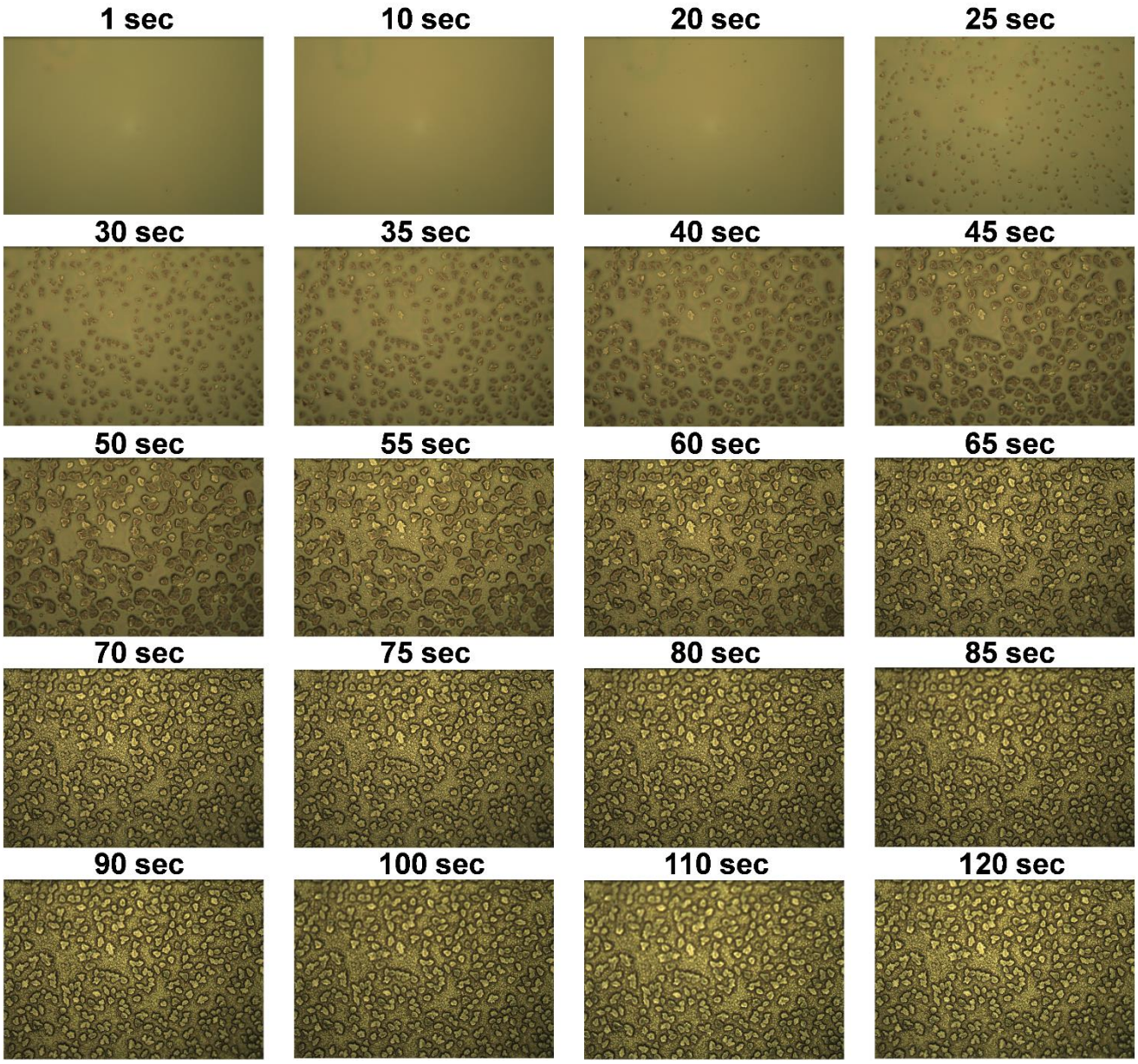

Figure S17: In-situ optical microscopy. Top-view optical microscope images of $MAPbI_{2.1}Br_{0.9}$ + 0.8% $FABF_4$ (Target 1) film at various stages of isothermal crystallization.

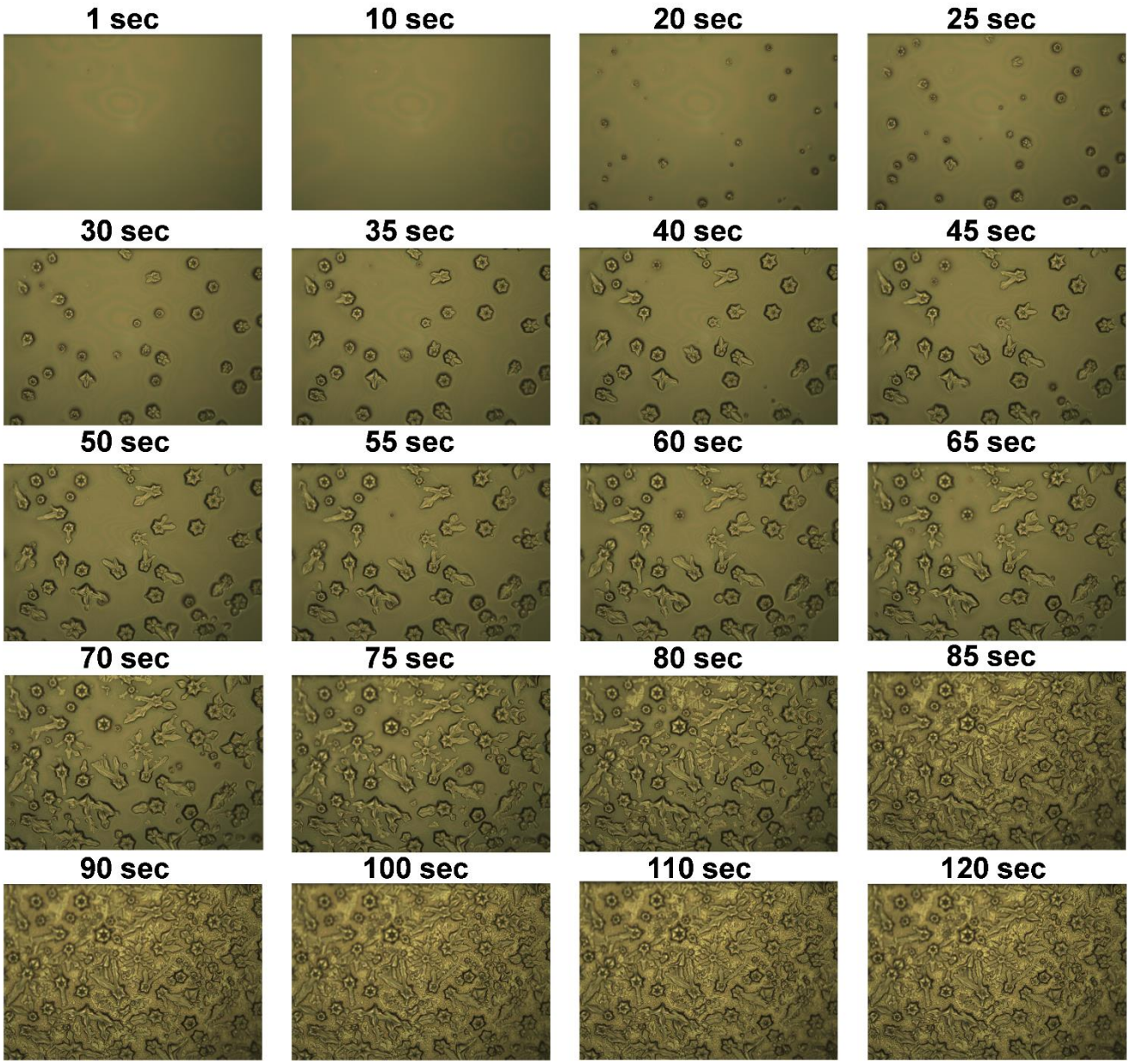

Figure S18: In-situ optical microscopy. Top-view optical microscope images of $MAPbI_{2.1}Br_{0.9}$ + 0.8% $PEABF_4$ (Target 2) film at various stages of isothermal crystallization.

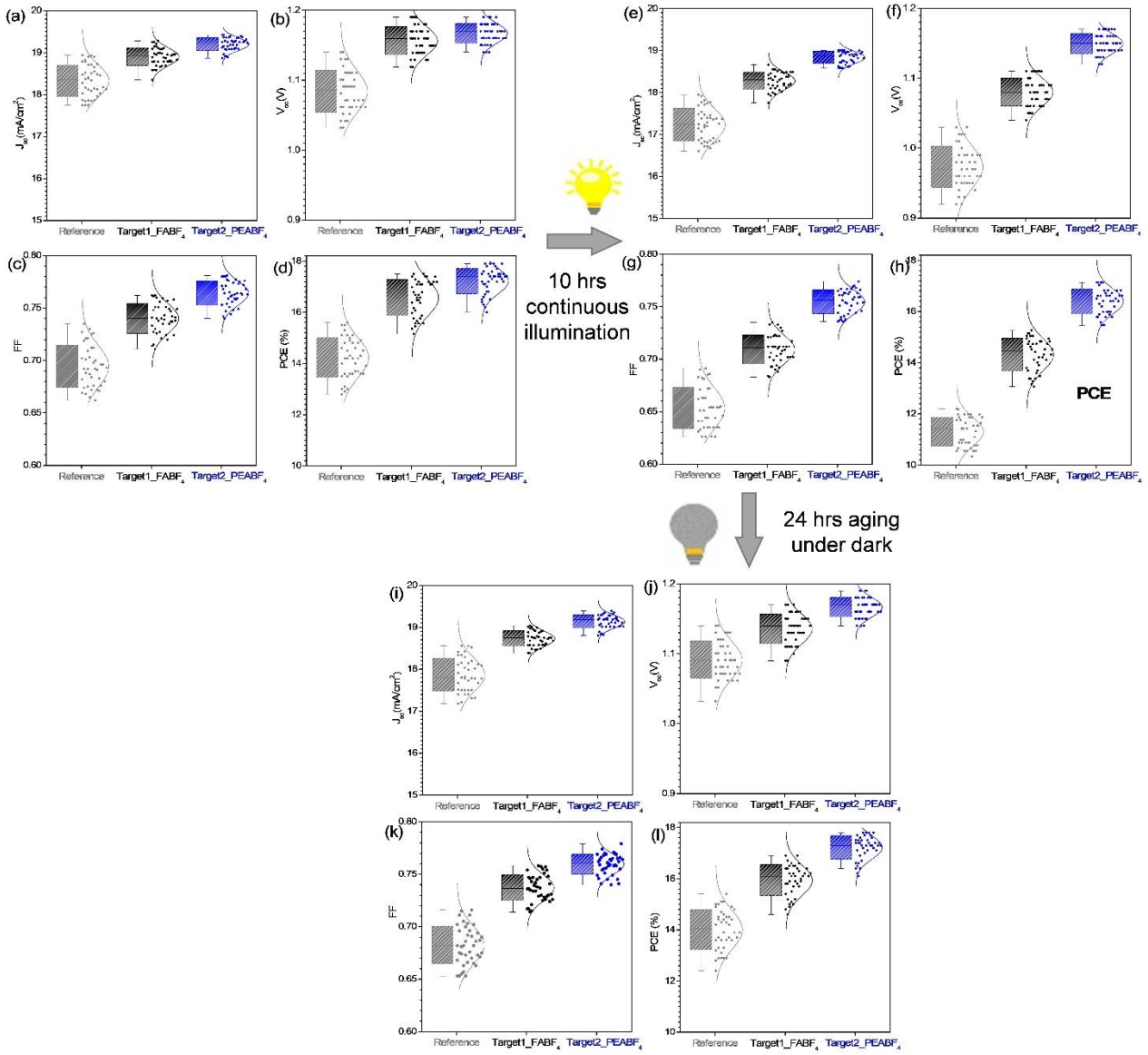

Figure S19: Statistics of J_{sc}, V_{oc}, FF and PCE from 40 devices for each Reference (gray), Target1 (black) and Target 2 (blue) (a-d) before illumination, (e-h) after 2 hours continuous illumination and (i-l) 24 hours in dark after 2 hour continuous illumination.

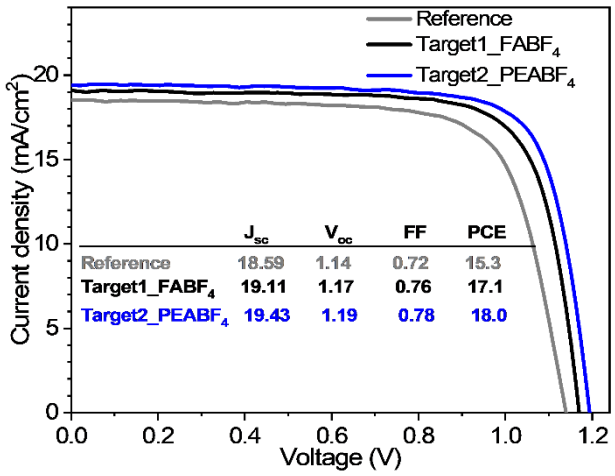

Figure S20: Current density–voltage (*J–V*) curves of $MAPbI_{2.1}Br_{0.9}$ (reference; gray), $MAPbI_{2.1}Br_{0.9}$ + 0.8% $FABF_4$ (target 1; black) and $MAPbI_{2.1}Br_{0.9}$ + 0.8% $PEABF_4$ (target 2; blue) showing initial performance for the stability test.

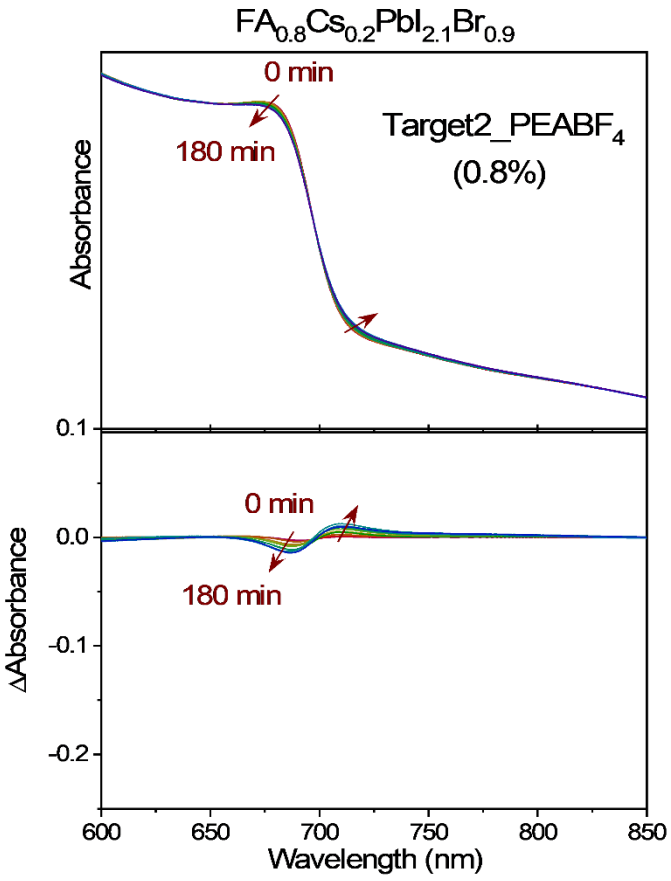

Figure S21: Absorption spectra (upper panel) and difference absorption spectra (lower panel) of $FA_{0.8}Cs_{0.2}PbI_{2.1}Br_{0.9}$ + 0.8% $PEABF_4$ film on FTO substrates. Here difference absorption spectra was obtained by subtracting the spectrum with no light spectrum.

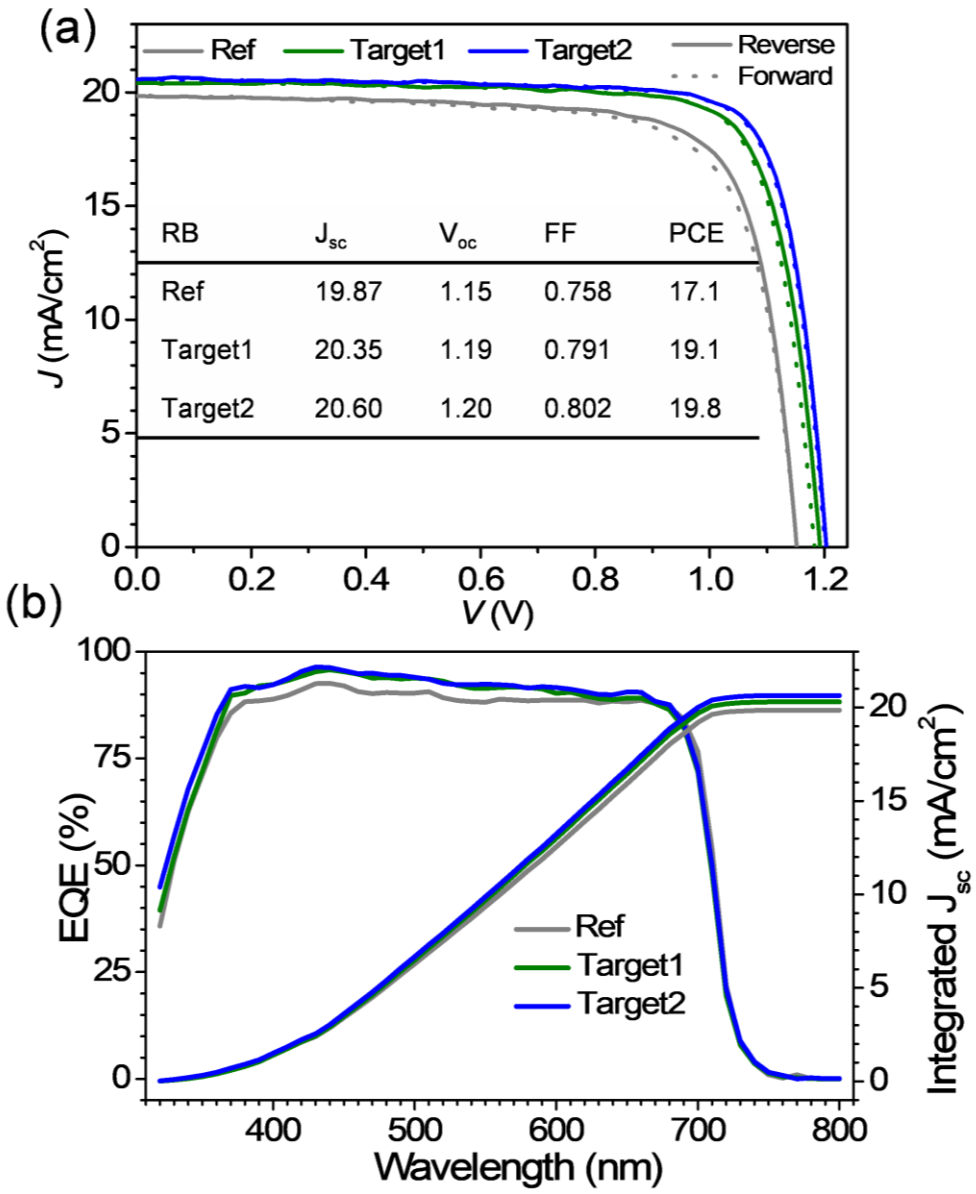

Figure S22: (a) Current density–voltage (*J–V*) curves of $FA_{0.8}Cs_{0.2}PbI_{2.1}Br_{0.9}$ (reference; gray), $FA_{0.8}Cs_{0.2}PbI_{2.1}Br_{0.9}$ + 0.8% $FABF_4$ (target 1; green) and $FA_{0.8}Cs_{0.2}PbI_{2.1}Br_{0.9}$ + 0.8% $PEABF_4$ (target 2; blue) with each champion cell (b) External Quantum Efficiency (EQE) and Integrated J_{sc} of the corresponding PSCs.

References:

1. Elmelund, T., Seger, B., Kuno, M. & Kamat, P. V. How Interplay between Photo and Thermal Activation Dictates Halide Ion Segregation in Mixed Halide Perovskites. *ACS Energy Lett.* **5**, 56–63 (2020).

2. Srivastava, V. *et al.* Study on the defect density of states in light soaking effect enhanced performance of perovskite solar cells. *J. Phys. D. Appl. Phys.* **52**, 265302 (2019).

3. Yang, G. *et al.* Defect engineering in wide-bandgap perovskites for efficient perovskite–silicon tandem solar cells. *Nat. Photonics* **16**, 588–594 (2022).

4. Seo, S. *et al.* An ultra-thin, un-doped NiO hole transporting layer of highly efficient (16.4%) organic–inorganic hybrid perovskite solar cells. *Nanoscale* **8**, 11403–11412 (2016).

5. Seo, S., Jeong, S., Bae, C., Park, N.-G. & Shin, H. Perovskite Solar Cells with Inorganic Electron- and Hole-Transport Layers Exhibiting Long-Term (approximately 500 h) Stability at 85 degrees C under Continuous 1 Sun Illumination in Ambient Air. *Adv. Mater.* **30**, 1801010 (2018).

6. Nandi, P. *et al.* Stabilizing Mixed Halide Lead Perovskites against Photoinduced Phase Segregation by A-Site Cation Alloying. *ACS Energy Lett.* **6**, 837–847 (2021).

7. Alghamdi, A. R. M., Yanagida, M., Shirai, Y., Andersson, G. G. & Miyano, K. Surface Passivation of Sputtered NiOx Using a SAM Interface Layer to Enhance the Performance of Perovskite Solar Cells. *ACS Omega* **7**, 12147–12157 (2022).

8. Gillespie, D. T. A general method for numerically simulating the stochastic time evolution of coupled chemical reactions. *J. Comput. Phys.* **22**, 403–434 (1976).

9. Gibson, M. A. & Bruck, J. Efficient Exact Stochastic Simulation of Chemical Systems with Many Species and Many Channels. *J. Phys. Chem. A* **104**, 1876–1889 (2000).